Journal of Petroleum Science and Engineering 164 (2018) 91–102

Contents lists available at ScienceDirect

Journal of Petroleum Science and Engineering

journal homepage: www.elsevier.com/locate/petrol

Microcrack-based geomechanical modeling of rock-gas interaction during supercritical CO_2 fracturing

Liyuan Liu [a,b], Wancheng Zhu [a,*], Chenhui Wei [a], Derek Elsworth [b], Jiehao Wang [b]

[a] Center for Rock Instability and Seismicity Research, Northeastern University, Shenyang, 110819, PR China
[b] Department of Energy and Mineral Engineering, EMS Energy Institute and G3 Center, Pennsylvania State University, University Park, PA, 16802, USA

ARTICLE INFO

Keywords:
Supercritical CO_2 fracturing
Gas adsorption
Internal swelling stress
Rock damage
Numerical simulation

ABSTRACT

Relative to water-based fluids, non-aqueous fracturing fluids have the potential to increase production, reduce water requirements, and to minimize environmental impacts. Since the viscosity of supercritical CO_2 is one-tenth that of water, its density is close to that of water, and is capable of promoting sorptive rejection of methane, it is an attractive substitute for water in the extraction of shale gas and coalbed methane. The following defines a geomechanical model accommodating the interaction of fluid flow, adsorption-induced swelling stress, solid deformation and damage to quantify rock-gas interactions during supercritical CO_2 fracturing for shale gas production. The architecture of the shale is accommodated that includes both pore- and micro-crack-based porosity. According to the microcrack model representing shales with low porosity, both analytical and numerical results show that the effective stress coefficient is much smaller than unity. We analyze the potential advantages of fracturing using supercritical CO_2 including enhanced fracturing and fracture propagation, increased desorption of methane adsorbed in organic-rich portions of the shale and the potential for partial carbon sequestration. Rock-gas interactions include both the linear poroelastic response and the chemo-mechanical interaction due to sorption. Simulation results demonstrate that supercritical CO_2 fracturing indeed has a lower fracture initiation pressure and a significantly lower breakdown pressure, as observed in experiments, and that fractures with greater complexity than those developed with liquid CO_2 and water fracturing result. With increasing dynamic viscosity of the fracturing fluids, the predicted breakdown pressure also increases, consistent with experimental observations.

1. Introduction

Hydraulic fracturing is used for the production of hydrocarbons but also for the recovery of deep geothermal fluids. The development of massive hydraulic fracturing has substantially increased shale oil and gas production, generated an energy boom in the US and significantly lowered hydrocarbon costs (Middleton et al., 2015; Yuan et al., 2015a, 2017). However, its use in low permeability (tight) gas reservoirs has presented significant challenges (Pijaudier-Cabot, 2013; Ye et al., 2017; Yuan et al., 2015b). The permeabilities of such reservoirs are typically in the nanodarcy range (10^{-21} m^2) prohibiting efficient recovery (Javadpour, 2009; Sheng et al., 2015; Wu et al., 2015). Mechanisms of gas recovery by hydraulic fracturing (Middleton et al., 2015) are shown in Fig. 1. These highlights that various length scales involved in shale gas production cover thirteen orders of magnitude, ranging from nanometer size pores where methane is trapped to kilometer-scale hydraulic fractures that are conduits to the production well (Davies et al., 2012).

Currently, water is the only fracturing fluid widely used in commercial shale gas and shale oil production. This is principally due to its low cost, availability, and its suitability for fracturing. However, a representative shale gas well needs to inject from 2 to 4 million gallons of water into the deep reservoir (API, 2010; Scanlon et al., 2014). In the initial stages of gas recovery, about 15%–80% of flow-back water is recovered (GWPC, 2009; EPA, 2010). Meanwhile, flow-back water is contaminated with secondary components, which are added to the water to induce fracture generation (Jackson et al., 2013). This flow-back water must be disposed, usually through deep re-injection into geologic formations. Large-scale water re-injection has been related to triggered seismicity that induces low-level earthquakes (Vidic et al., 2013; Ellsworth, 2013; Elsworth et al., 2016). In this respect, using non-aqueous fluids is promising to solve large volumes of water re-injection. In addition, water from the conventional water-based fracturing fluids will be trapped in the

* Corresponding author. Center for Rock Instability and Seismicity Research, P.O. Box 138, Northeastern University, Shenyang, 110819, PR China.
E-mail address: zhuwancheng@mail.neu.edu.cn (W. Zhu).

https://doi.org/10.1016/j.petrol.2018.01.049
Received 25 September 2017; Received in revised form 5 January 2018; Accepted 24 January 2018

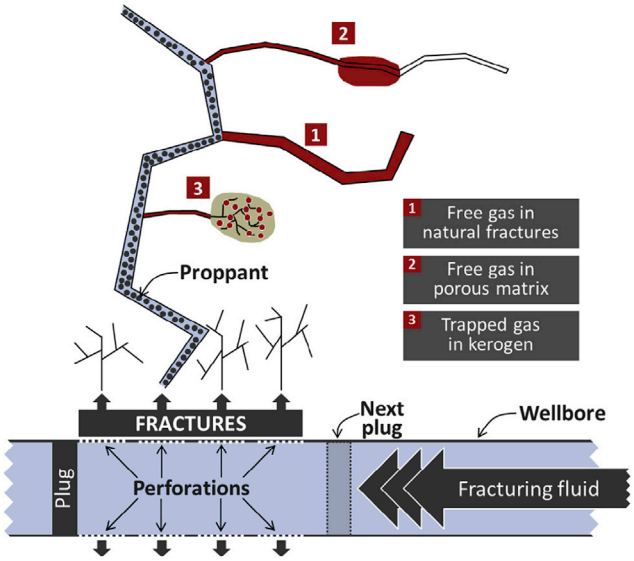

Fig. 1. Schematic of a fracturing system highlighting induced and natural fractures and three primary gas-in-place origins of methane. An alternative fracturing fluid such as CO_2 may more efficiently extract gas from (1) and (2) since CO_2 is miscible with hydrocarbons thereby preventing multi-phase flow blocking and from (3) since CO_2 can exchange with methane that is absorbed in the kerogen (Middleton et al., 2015).

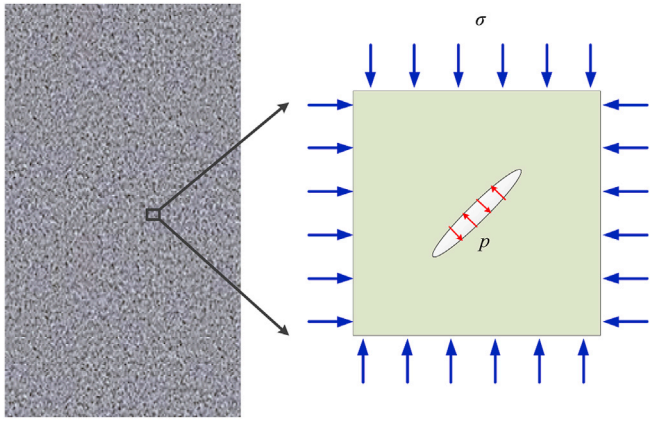

Fig. 2. Illustration of the single crack microelement.

near-wellbore region during the fracturing processes, which may impede gas to flow to the wells. This adverse effect is observed in many reservoirs (Al-Anazi et al., 2002; Mahadevan et al., 2007; Parekh and Sharma, 2004). For these reasons, reducing the use of water in hydraulic fracturing is a high priority for industry, policy makers, and concerned environmental groups. This possible reduction has stimulated investigation into the use of non-aqueous fracturing fluids, including hydrocarbons and supercritical CO_2 (Wang et al., 2012, 2015).

The fracture path and breakdown pressure vary with the composition and state of the fracturing fluid (Ishida et al., 2012; Alpern et al., 2012; Gan et al., 2015). Therefore, determining the mechanics of these interactions is important. The penetration of the fracturing fluid within the network of existing cracks depends directly on its viscosity and interfacial characteristics. By reducing the resistance indexed through these parameters, fluids will penetrate more easily in the existing cracks and apply pressure to reactivate them. Thus, the issue is to determine the "right" fluid. There are many candidate fluids, including propane, nitrogen and carbon dioxide.

Supercritical CO_2 is one such potential fluid. CO_2 is of potential interest as a class of energized fluid or foam, particularly as the drawbacks of conventional fracturing fluids become more obvious (Gupta and Bobier, 1998; Gupta, 2011). Supercritical CO_2 offers several significant advantages over water, as well as some potential drawbacks. Key potential advantages for CO_2 contain increased methane (CH_4) and hydrocarbon production, reduced pressurization requirements, enhanced fracturing properties, effective gas displacement from fractures, enhanced desorption of CH_4 from organics and the reduction or

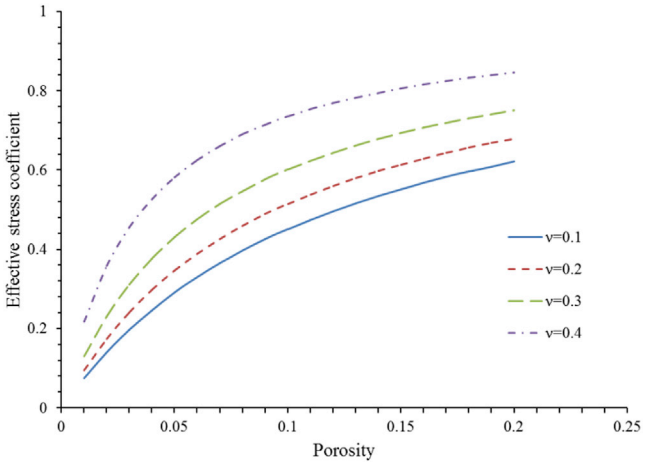

Fig. 4. Changes in effective stress coefficient with porosity and Poisson ratio.

Table 1
The impact of β and ν on effective stress coefficient at $\phi = 0.01$.

	$\beta = 1/10$	$\beta = 1/15$	$\beta = 1/20$	$\beta = 1/25$
$\nu = 0.1$	0.0762	0.1101	0.1416	0.171
$\nu = 0.2$	0.0964	0.1379	0.1758	0.2105
$\nu = 0.3$	0.1317	0.1853	0.2327	0.2749
$\nu = 0.4$	0.2188	0.2958	0.359	0.4118

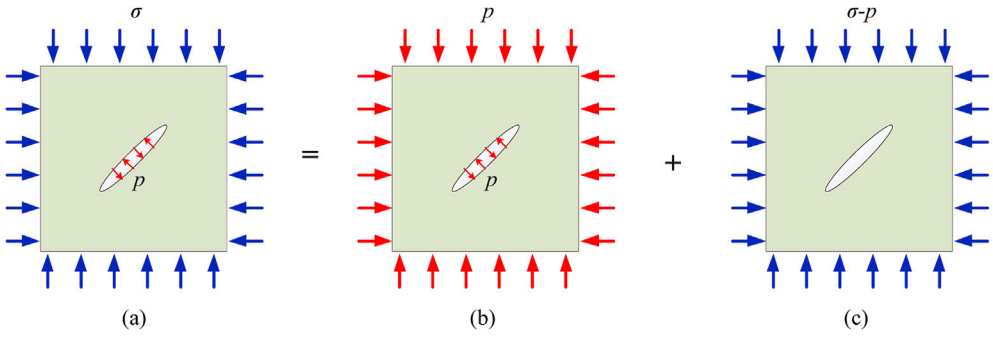

Fig. 3. Illustration of superposition principle.

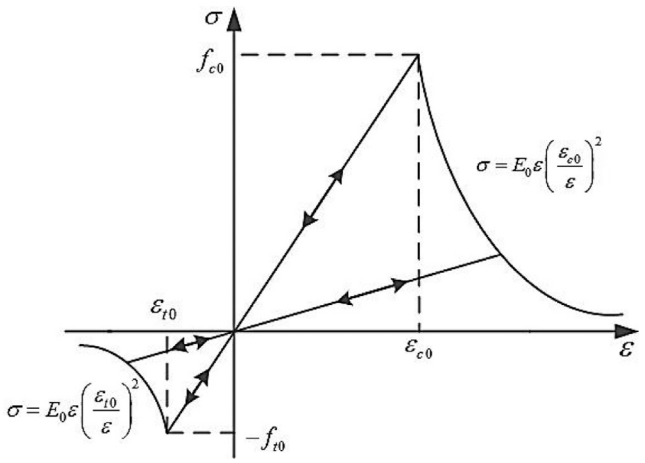

Fig. 5. The constitutive law of rock under uniaxial stress condition.

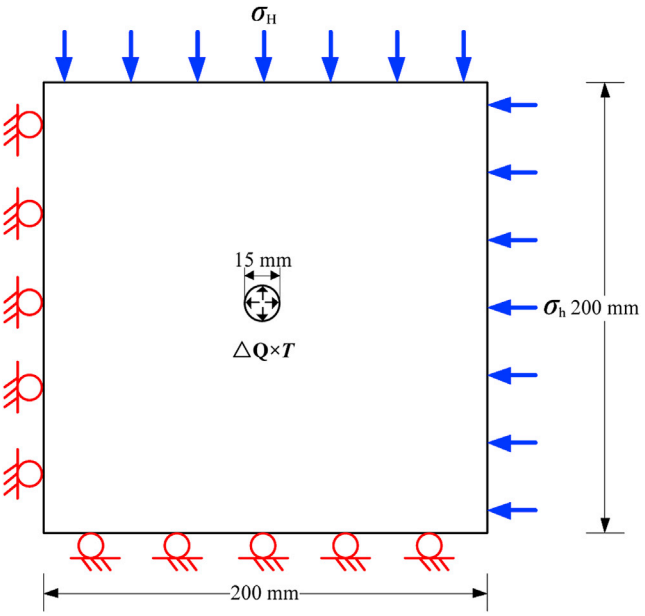

Fig. 6. Numerical model for fracturing experiments.

elimination of injection and flow-back water (Middleton et al., 2015). Furthermore, if CO_2 is an effective fracturing fluid, then shale gas reservoirs would likely become a major utilization option for carbon storage.

Specifically, CO_2 could expand production through enhanced fracturing and fracture propagation, reduced flow-blocking to gas flow by the fracturing fluid and increased desorption of methane adsorbed in organic-rich parts of the shale (Jung et al., 2015; Heller and Zoback, 2014). Moreover, CO_2-based fracturing offers the potential for CO_2 sequestration (Stauffer et al., 2011; Middleton et al., 2012; Li and Elsworth, 2015) both during the fracturing phase and after production has concluded. Thus, supercritical CO_2 is a promising alternative to water for shale gas fracturing (Middleton et al., 2014).

In the past few years, many researchers have made constant efforts to investigate the fracturing process based on the numerical simulation method with various models, which mainly including complex fracture network (CFN) model (Olson, 2008; Ren et al., 2016), discrete fracture network (DFN) model based on discrete element method (Rogers et al., 2010), and cohesive zone model (CZM) (Elices et al., 2002). These models reveal the important role of viscous flow on rock stress distribution and have the capability to predict hydraulic fracture propagation

Table 2
Physico-mechanical parameters for simulations.

Symbol	Value	Physical meanings	Unit
m	10	Homogeneity index	
$\bar{E}_0$	33	Mean value of the elasticity modulus	GPa
$\bar{f}_c$	190	Mean value of uniaxial compressive strength	MPa
$\bar{f}_t$	23	Mean value of uniaxial tensile strength	MPa
ν	0.35	Poisson ratio	–
ϕ_0	0.01	Initial porosity	–
k_0	1.0×10^{-18}	Initial permeability	m^2
μ_{l-CO_2}	7.46×10^{-5}	Dynamic viscosity of liquid CO_2	Pa·s
μ_{SC-CO_2}	2.03×10^{-5}	Dynamic viscosity of supercritical CO_2	Pa·s
μ_w	4.688×10^{-4}	Dynamic viscosity of water	Pa·s
P_L	2.3	Langmuir pressure constant for supercritical CO_2	MPa
ε_L	0.035	Langmuir strain constant for supercritical CO_2	–
V_L	0.02702	Langmuir volume constant for supercritical CO_2	m^3/kg
p_0	101.325	Initial pore pressure	KPa

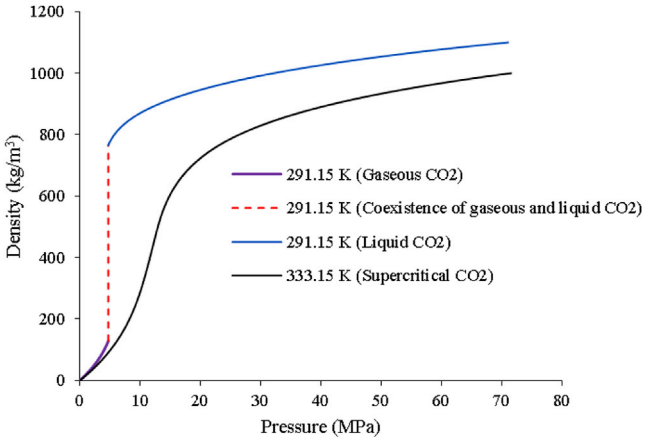

Fig. 7. Density-pressure curves under experimental conditions.

behaviors, they assume the rock is homogeneous and elastic, which is generally not the case of the formation rocks. In this study, a fully coupled hydraulic-geomechanical fracture model has been built. In this modeling, the concept of FEM-based damage mechanics, that combine the maximum tensile stress theory and the Mohr-Coulomb theory, is introduced together to predict fracture propagation behavior in heterogeneous rocks.

The following addresses the potential effectiveness of using supercritical CO_2 as an alternative fracturing fluid for shale gas production, including a comparison between fracturing via supercritical CO_2, liquid CO_2, and water. A coupled model of mechanics, rock damage and gas flow is proposed to explore key gas fracturing processes, in which an equation-of-state of CO_2 is included. This inclusion is essential to explore the roles of rock-gas interactions on the progressive propagation of fractures and to demonstrate whether and how supercritical CO_2 could significantly increase shale gas production.

2. Pore and microcrack model

Shale is a clastic sedimentary rock that has lithified during burial and diagenesis. These processes control the evolved pore-structure and architecture that in turn affect gas generation, adsorption and migration. The following documents a microcrack model that accurately defines this architecture and resulting mechanical response.

The concept of effective stress is useful in describing the effect of pore pressure on the mechanical response of porous materials. Following

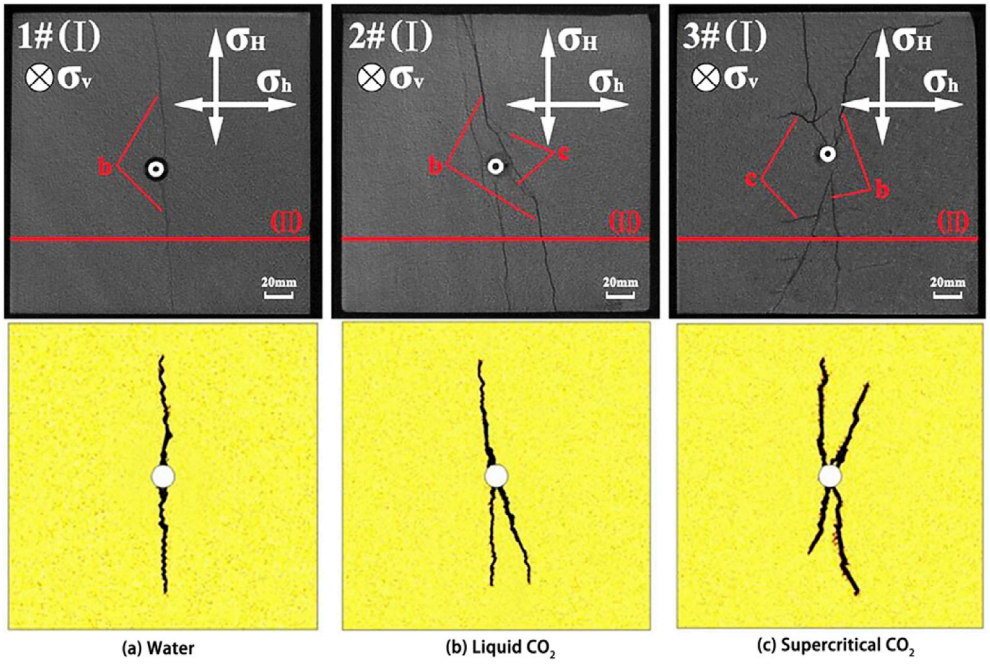

Fig. 8. Fracture patterns obtained from experiments (upper) (Zhang et al., 2017) and numerical simulations (lower) during injection of different fracturing fluids. (a) Shale specimen fractured with water, (b) shale specimen fractured with liquid CO_2. (c) Shale specimen fractured with supercritical CO_2.

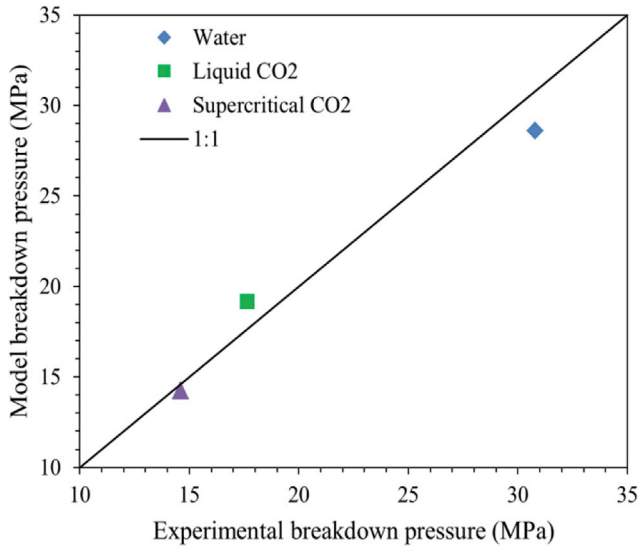

Fig. 9. Comparisons of breakdown pressure between experimental and numerical results.

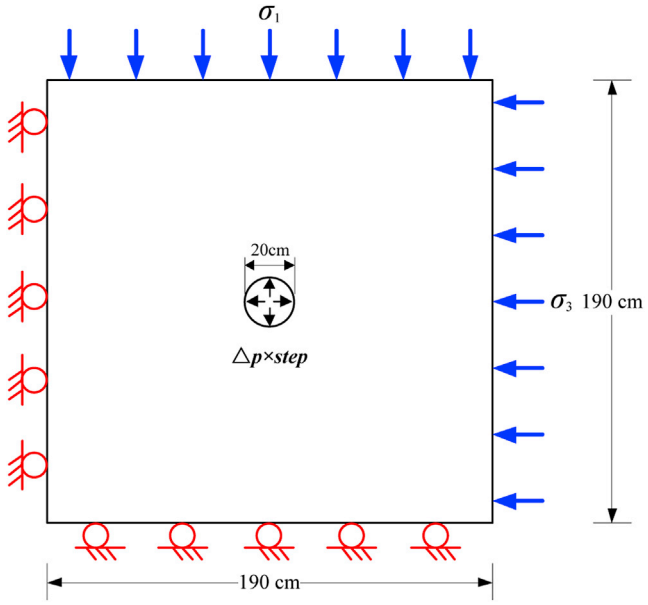

Fig. 10. The numerical model of fluid fracturing.

Terzaghi (1923), Biot (1941), Walsh (1965), Nur and Byerlee (1971), Carroll (1979), and others, we propose a narrow microcrack model to represent rock with low porosity. As shown in Fig. 2, the total stress, σ, is applied on the external boundaries of a microelement, and pore pressure, p, is applied internally. Assuming that cracks in the shale are sparse and are distributed randomly, each microelement contains a single crack. Therefore, the interactions between microcracks are ignored.

We first, analyze the deformation of a microelement, under the combined action of total stress and pore pressure. From Fig. 3, the deformation caused by total stress and pore pressure can be decomposed by the superposition of deformations (see Fig. 3(b) and (c)) resulting from hydrostatic pressure, p, and external stress, σ-p, respectively.

Thus, the volume strain of the microelement (see Fig. 3(c)) is:

$$\frac{\Delta_c v_t}{v_t} = \frac{\sigma - p}{K_1} + \frac{\Delta_c v_p}{v_t} \tag{1}$$

where v_t is the total volume of the microelement (see Fig. 3(c)) and v_p is the crack volume. The strain energy of the crack is:

$$w_c = (\sigma - p)\Delta_h v_p \tag{2}$$

Combining Eq. (1) and Eq. (2) yields

$$\frac{\Delta_c v_t}{v_t} = \frac{\sigma - p}{K_1} + \frac{w_c}{(\sigma - p)v_t} \tag{3}$$

Applying the principle of superposition yields the whole volume strain of the microelement (see Fig. 3(a)):

$$\frac{\Delta_a v_t}{v_t} = \frac{\sigma}{K_1} + \frac{w_c}{(\sigma - p)v_t} \tag{4}$$

Table 3
Physico-mechanical parameters of rock and fluids.

Symbol	Value	Physical meanings	Unit
m	5	Homogeneity index	
$\bar{E}_0$	22	Mean value of the elasticity modulus	GPa
$\bar{f}_c$	200	Mean value of the uniaxial compressive strength	MPa
$\bar{f}_t$	25	Mean value of the uniaxial tensile strength	MPa
ν	0.33	Poisson ratio	–
ϕ_0	0.01	Initial porosity	–
k_0	1.0×10^{-19}	Initial permeability	m^2
μ_{g-CO_2}	1.38×10^{-5}	Dynamic viscosity of gaseous CO_2	Pa·s
μ_{l-CO_2}	9.25×10^{-5}	Dynamic viscosity of liquid CO_2	Pa·s
μ_{SC-CO_2}	4.04×10^{-5}	Dynamic viscosity of supercritical CO_2	Pa·s
μ_w	1.0×10^{-3}	Dynamic viscosity of water	Pa·s
P_L	2.12	Langmuir pressure constant for supercritical CO_2	MPa
ε_L	0.047	Langmuir strain constant for supercritical CO_2	–
V_L	0.03226	Langmuir volume constant for supercritical CO_2	m^3/kg
p_0	0.1	Initial pore pressure	MPa

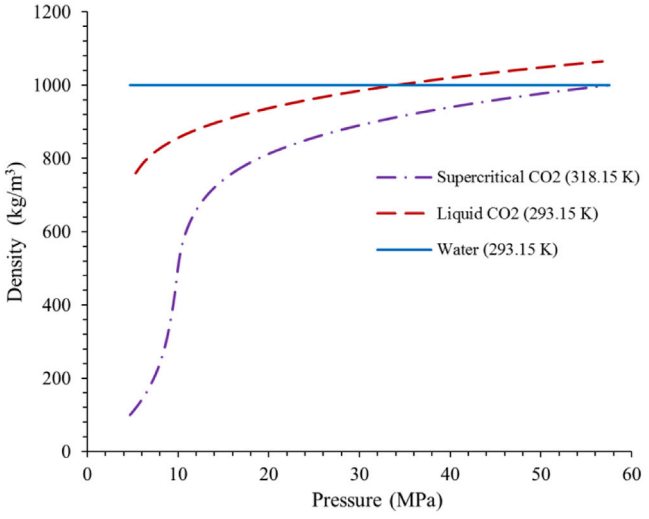

Fig. 11. The density-pressure curves of CO_2 for numerical input.

The volume increment of the microelement is:

$$\Delta_a v_t = \frac{\sigma}{K_I} v_t + \frac{w_c}{\sigma - p} \tag{5}$$

Summing of all volume increments of the microelements, the total volume increment can be expressed as:

$$\Delta_a V_t = \sum \Delta_a v_t = \frac{\sigma}{K_I} \sum v_t + \frac{1}{\sigma - p} \sum w_c = \frac{\sigma}{K_I} V_t + \frac{1}{\sigma - p} \sum w_c \tag{6}$$

The total volume strain is:

$$\frac{\Delta_a V_t}{V_t} = \frac{\sigma}{K_I} + \frac{1}{(\sigma - p) V_t} \sum w_c \tag{7}$$

Under condition of plane strain, the strain energy of a narrow elliptical crack loaded by external stress, σ-p, is (Griffith, 1921)

$$w_c = \frac{2\pi(1-\nu^2)(\sigma - p)^2 c^3}{3K_I(1-2\nu)} \tag{8}$$

where c is half-length of the fracture (narrow elliptical crack).

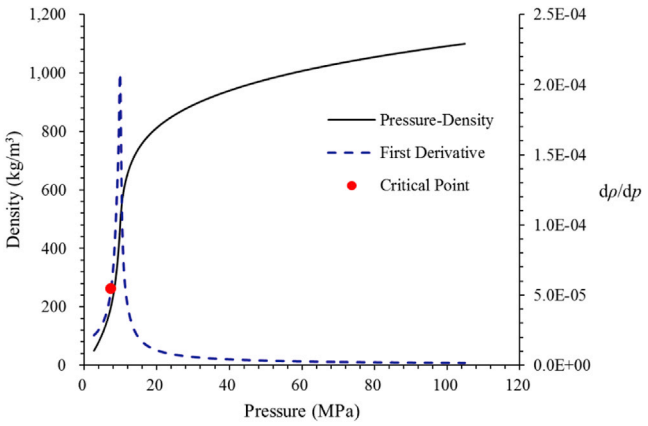

Fig. 12. The density-pressure curve of supercritical CO_2 and its first derivative.

$$\frac{\Delta_a V_t}{V_t} = \frac{\sigma}{K_I} + \frac{2\pi(1-\nu^2)(\sigma - p)}{3K_I(1-2\nu)V_t} \sum c^3 \tag{9}$$

Defining the average crack length and average microelement volume, then, $N\bar{c}^3 = \sum_N c^3$, $N\bar{v}_t = \sum_N v_t = V_t$, and Eq. (9) can be written as:

$$\frac{\Delta_a V_t}{V_t} = \frac{\sigma}{K_I} + \frac{2\pi(1-\nu^2)(\sigma - p)\bar{c}^3}{3K_I(1-2\nu)\bar{v}_t} \tag{10}$$

Assuming that the thickness of the element is c, the volume of the elliptical crack is $\pi\beta c^3$. Therefore, the porosity can be written as $\phi = \pi\beta\bar{c}^3/\bar{v}_t$. β is the aspect ratio of the crack. The total volume strain can thus be expressed as:

$$\frac{\Delta_a V_t}{V_t} = \frac{\sigma}{K_I}\left[1 + \frac{2\phi(1-\nu^2)}{3\beta(1-2\nu)}\right] - \frac{2\phi(1-\nu^2)}{3K_I\beta(1-2\nu)} p \tag{11}$$

Arranging Eq. (11) into the form of effective stresses:

$$\frac{K_I}{1 + \frac{2\phi(1-\nu^2)}{3\beta(1-2\nu)}} \frac{\Delta_a V_t}{V_t} = \sigma - \left(1 - \frac{1}{1 + \frac{2\phi(1-\nu^2)}{3\beta(1-2\nu)}}\right) p \tag{12}$$

Finally, this expression defines the effective stress coefficient as:

$$\alpha = 1 - \frac{1}{1 + \frac{2\phi(1-\nu^2)}{3\beta(1-2\nu)}} \tag{13}$$

According to Fig. 4, the effective stress coefficient increases with an increase in porosity but asymptotes at high porosities and increases with Poisson ratio (see Fig. 4 and Table 1). As indicated in Table 1, the effective stress increases with the aspect ratio of the cracks. Importantly, for shales with low porosity, both the analytical and numerical results show that the effective stress coefficient is much smaller than 1.

3. Governing equations

During fluid-driven fracturing, supercritical CO_2 will penetrate into the rock around borehole easier and faster than higher viscosity and interfacial tension fluids. The initiation and evolution of fluid-driven fractures is a coupled phenomenon involving fluid flow, solid deformation and damage. In the following, a set of governing equations are developed for rock deformation and fluid flow that represent the macroscopic scale and include the definition of a damage evolution law (Zhu and Tang, 2004).

3.1. Deformation

From poroelasticity theory, the constitutive relation for the deformed

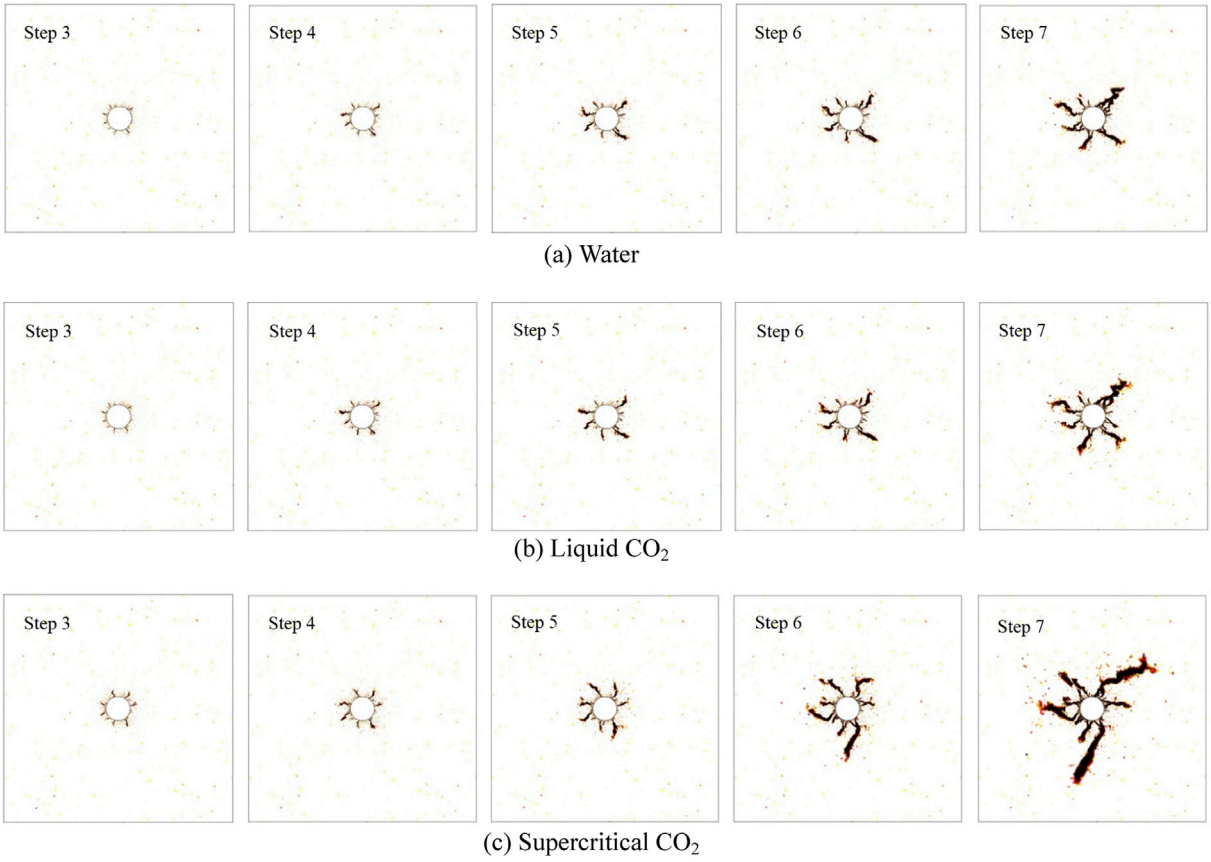

Fig. 13. Fracturing patterns under different injected fluids when lateral pressure coefficient $\lambda = 1$.

rock may be expressed as:

$$\varepsilon_{ij} = \frac{1}{2G}\sigma_{ij} - \left(\frac{1}{6G} - \frac{1}{9K}\right)\sigma_{kk}\delta_{ij} + \frac{\alpha}{3K}p\delta_{ij} + \frac{1}{3}\varepsilon_s\delta_{ij} \tag{14}$$

where G is the shear modulus of the rock, K is the bulk modulus, p is the pore pressure, α is the effective stress coefficient, δ_{ij} is the Kronecker delta and ε_s is the gas sorption-induced strain.

Applying the Langmuir isotherm to obtain the gas sorption-induced strain yields:

$$\varepsilon_s = \frac{\varepsilon_L p}{p + P_L} \tag{15}$$

where ε_L is the Langmuir strain constant and P_L is the Langmuir pressure constant.

From this, the Navier-type constitutive relation may be expressed as:

$$Gu_{i,jj} + \frac{G}{1-2\nu}u_{j,ji} - \alpha p_{,i} - K\varepsilon_{s,i} + f_{,i} = 0 \tag{16}$$

where Eq. (16) is the governing equation for rock deformation.

3.2. CO_2 flow in fracture networks

Gas exists in both free-phase and absorbed states. The gas mass can be thus defined as:

$$m = \phi\rho + \rho_{ga}\rho_c\frac{V_L p}{p + P_L} \tag{17}$$

where ρ is the gas density under fracturing pressure, ρ_{ga} is the gas density at atmospheric pressure, ρ_c is the density of the rock, V_L is the Langmuir volume constant and P_L is the Langmuir pressure constant.

The first term on the right-hand side represents the free-phase gas in the fractures and the second the adsorbed gas. The loading induced by supercritical CO_2 injection includes both the poromechanical effect and the swelling effect. Despite responding to two distinct mechanisms, rock damage ensues in exactly the same way.

Applying mass conservation and the Darcy velocity to the gas phase gives:

$$\frac{\partial m}{\partial t} + \nabla\cdot\left(-\frac{k}{\mu}\rho\nabla p\right) = Q_s \tag{18}$$

where m is the gas content in the rock, k is the fracture permeability, μ is viscosity and Q_s is a gas source or sink. Substituting Eq. (17) into Eq. (18) yields the governing equation of gas flow in the fracture networks as:

$$\left(\phi\frac{\partial\rho}{\partial p} + \frac{\rho_{ga}\rho_c V_L P_L}{(p+P_L)^2}\right)\frac{\partial p}{\partial t} + \nabla\cdot\left(-\frac{k}{\mu}\rho\nabla p\right) = Q_s \tag{19}$$

Under the isothermal condition, the CO_2 density varies significantly with pressure but may be described to considerable accuracy through the equation of state proposed by Span and Wagner (1996). The Span-Wagner EOS explicitly includes the Helmholtz free energy but the CO_2 density is only related to the residual part of it, which can be written as:

$$\varphi^r(\delta,\tau) = \sum_{i=1}^{7} n_i\delta^{d_i}\tau^{t_i} + \sum_{i=8}^{34} n_i\delta^{d_i}\tau^{t_i}e^{-\delta^{c_i}} + \sum_{i=35}^{39} n_i\delta^{d_i}\tau^{t_i}e^{-\alpha_i(\delta-\varepsilon_i)^2-\beta_i(\tau-\gamma_i)^2} + \sum_{i=40}^{42} n_i\Delta^{b_i}\delta e^{-C_i(\delta-1)^2-D_i(\tau-1)^2} \tag{20}$$

where $\delta = \rho/\rho_c$ is the reduced density, $\tau = T_c/T$ is the inverse reduced temperature, $\Delta = \{(1-\tau) + A_i[(\delta-1)^2]^{1/(2\beta_i)}\}^2 + B_i[(\delta-1)^2]^{a_i}$, ρ_c is the

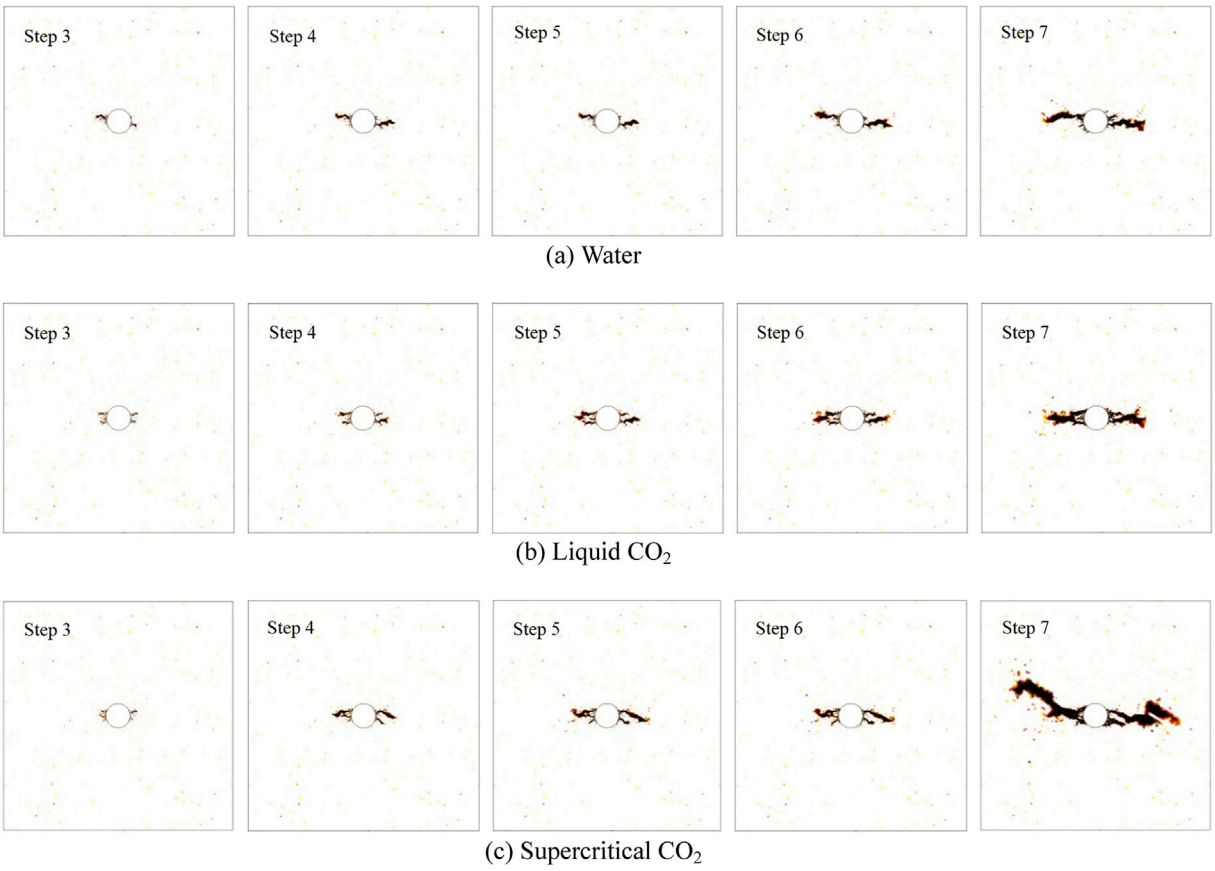

Fig. 14. Fracturing patterns under different injected fluids when lateral pressure coefficient $\lambda = 2$.

critical density, T_c is the critical temperature and the other parameters are all constants, the coefficients are selected from Span and Wagner (1996).

The fundamental equation of CO_2 given in this study is expressed in form of the Helmholtz free energy A with the two independent variables density ρ and temperature T. The dimensionless Helmholtz free energy $\phi = A/(RT)$ is commonly split into a part depending on the ideal-gas behavior ϕ^0 and a part which takes into account the residual fluid behavior ϕ^r. Since the Helmholtz free energy as a function of density and temperature is one form of a fundamental equation, all the thermodynamic properties of CO_2 can be obtained. The relation between CO_2 density and pressure can be defined as (Span, 2000):

$$p(\delta, \tau) = \left(1 + \delta\varphi_\delta^r\right)(\rho RT) \tag{21}$$

Where φ_δ^r is the derivative of the residual part of the Helmholtz free energy with respect to the reduced density and R is the universal gas constant.

Since the density of CO_2 cannot be calculated analytically from Eqs. (20) and (21), we use a numerical method. We use cubic spline interpolation to obtain the relationship between density and pressure and define the density-pressure curve as shown as Fig. 4. This is used on the distributed parameter model.

3.3. Water flow in fracture networks

Applying mass conservation and inserting the Darcy velocity for the water phase, the governing equation for water flow in the fracture network can be expressed as:

$$\frac{\partial m}{\partial t} + \nabla\cdot\left(-\frac{k}{\mu}\rho_w\nabla p\right) = Q_s \tag{22}$$

where m is the mass of water in the rock, ρ_w is the water density and Q_s is a source or sink.

Assuming that the rock is water saturated, the fluid mass can be expressed as $m = \rho_w\phi$ where ϕ is rock porosity. The rock compressibility can be expressed as $c_p = \frac{1}{\phi}\frac{d\phi}{dp}$, and the water compressibility coefficient as $c_w = \frac{1}{\rho_w}\frac{d\rho_w}{dp}$. Thus, the total compressibility coefficient is $c_t = c_p + c_w$.

Combining these relations yields the water flow equation expressed as:

$$\phi c_t\frac{\partial p}{\partial t} + \nabla\cdot\left(-\frac{k}{\mu}\nabla p\right) = Q_s \tag{23}$$

3.4. Damage evolution law

The nonlinear stress-strain relation for the rock under the conditions of uniaxial tension and compression can be simplified as a piecewise function, as shown in Fig. 5 (positive for compression). Damage in tension or shear is initiated when the stress state in an REV satisfies the maximum tensile stress criterion or the Mohr-Coulomb criterion respectively, as (Zhu and Tang, 2004):

$$F_1 = -\sigma_3 - f_{t0} = 0 \text{ or } F_2 = \sigma_1 - \sigma_3\frac{1+\sin\theta}{1-\sin\theta} - f_{c0} = 0 \tag{24}$$

where σ_1 and σ_3 are the maximum and minimum principal stresses, respectively, f_{t0} and f_{c0} are the uniaxial tensile and compressive strengths, respectively, θ is the internal frictional angle, F_1 and F_2 are two damage threshold functions.

The elastic modulus of an REV will decrease monotonically with the evolution of damage and may be expressed as:

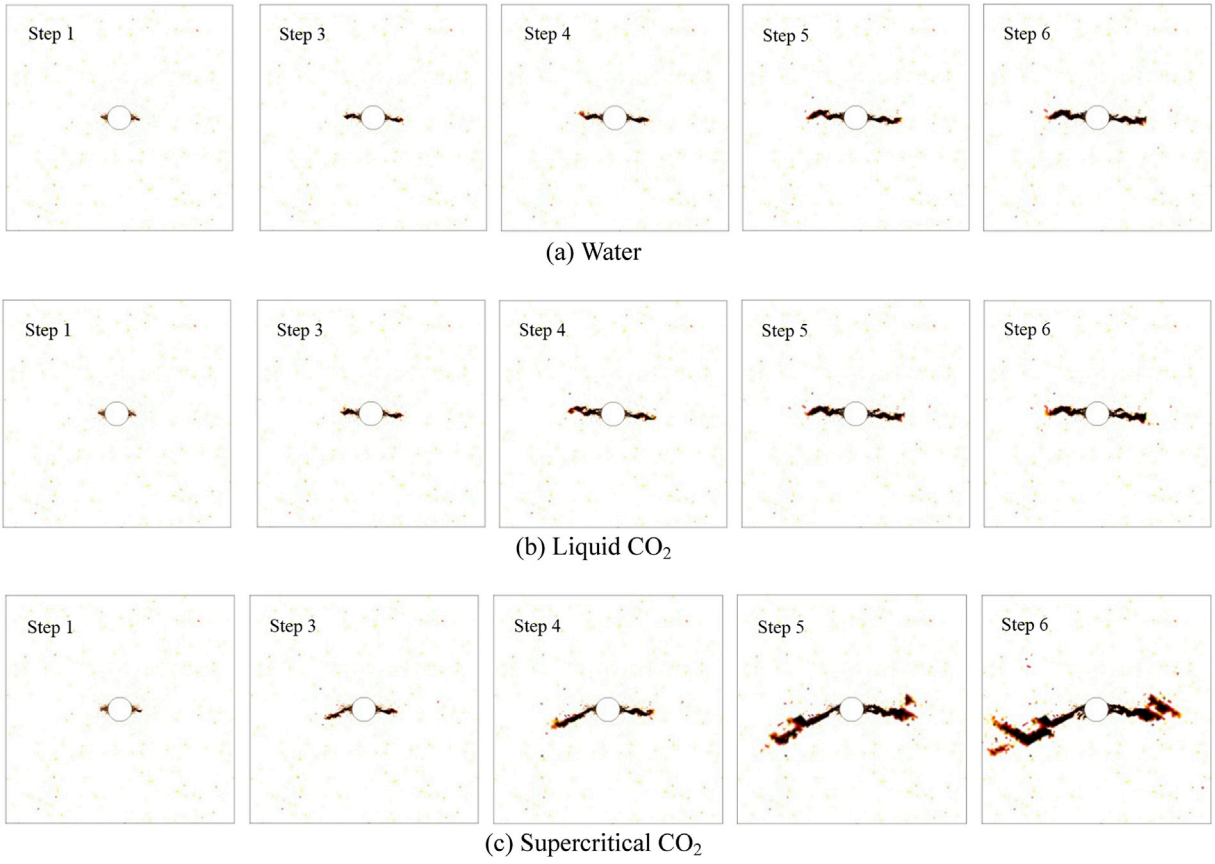

Fig. 15. Fracturing patterns under different injected fluids when lateral pressure coefficient $\lambda = 5$.

$$E = (1 - D)E_0 \tag{25}$$

where E_0 and E are the elastic modulus of an REV both before and after the initiation of damage and D is the damage variable (0–1). According to the constitutive law, as illustrated in Fig. 5, the damage variable can be defined as (Zhu et al., 2018):

$$D = \begin{cases} 0 & F_1 < 0 \quad and \quad F_2 < 0 \\ 1 - \left(\dfrac{\varepsilon_{t0}}{\varepsilon_3}\right)^2 & F_1 = 0 \quad and \quad dF_1 > 0 \\ 1 - \left(\dfrac{\varepsilon_{c0}}{\varepsilon_1}\right)^2 & F_2 = 0 \quad and \quad dF_2 > 0 \end{cases} \tag{26}$$

where ε_{t0} and ε_{c0} are maximum tensile and compressive principal strains, respectively. In the numerical implementation of Eq. (24), the tensile damage is checked first with the maximum tensile stress criterion, and only the REVs that are not damaged in tensile mode will be evaluated as to whether they are damaged in shear, or not, via the Mohr-Coulomb criterion.

After the initiation of damage, some other physico-mechanical parameters will change as the damage evolves. Eq. (25) represents the impact of damage on the elastic modulus of the medium with the permeability also a sensitive function of damage. Since the evolution of permeability with damage is complex, here we describe this relation as the following exponential function:

$$k = k_0 \exp(\alpha_k D) \tag{27}$$

where k_0 is the initial permeability and α_k is 5.0, representing a so-called damaged-permeability effect coefficient to indicate the effect of damage on the permeability.

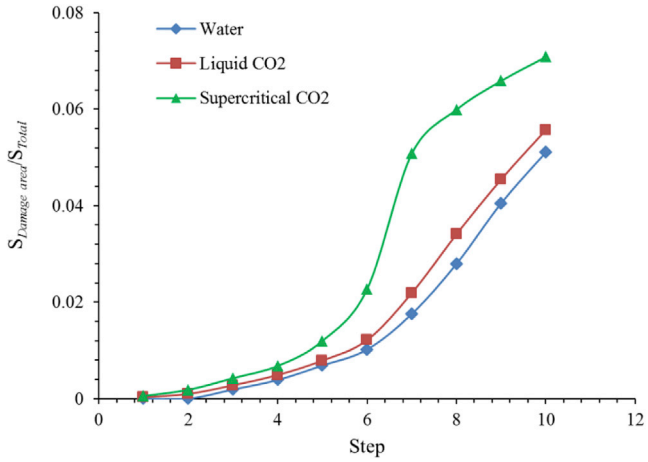

Fig. 16. The variations of $S_{Damage\ area}/S_{Toal}$ at different load steps during the injection of water, liquid CO_2, and supercritical CO_2.

4. Verification against experimental observations

The proposed numerical model is validated against observations of supercritical CO_2 fracturing (Zhang et al., 2017). The geometries and loading conditions of the shale specimen are defined as shown in Fig. 6. The cubic shale specimen is 200 mm on edge with a 15 mm diameter borehole. The experiments were conducted under different horizontal stress conditions using water, liquid CO_2, and supercritical CO_2 as fracturing fluids. The boundary conditions correspond to confining pressure $\sigma_H = 10$ MPa applied on the top boundary and $\sigma_h = 8$ MPa applied on the

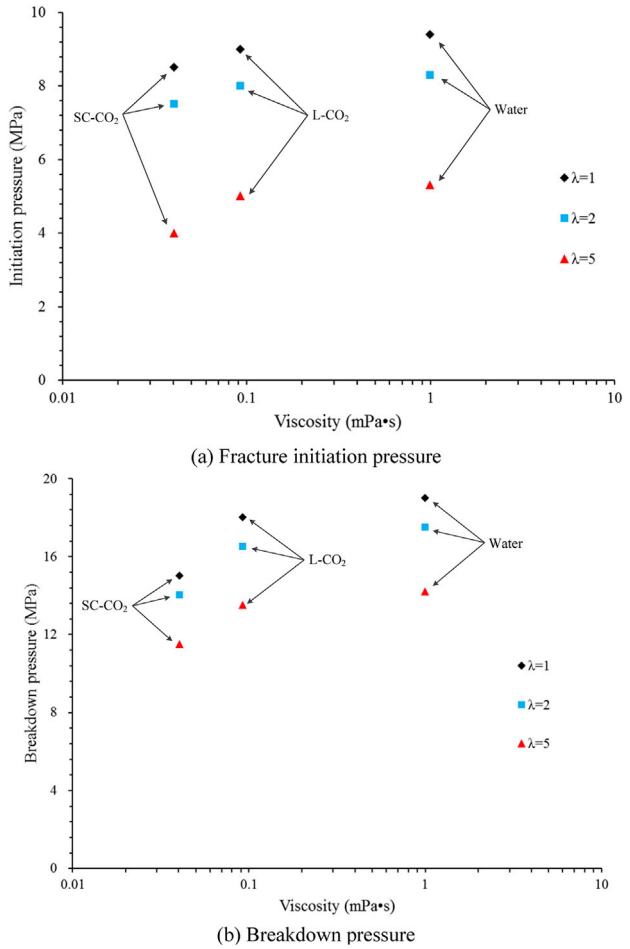

Fig. 17. The initiation and breakdown pressures during injection of water, liquid CO_2 and supercritical CO_2.

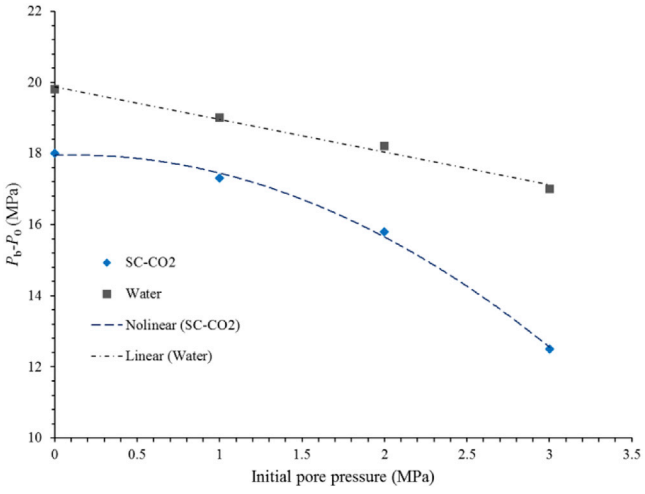

Fig. 18. The relationship between breakdown pressure and initial pore pressure.

right boundary with rollers along the left side and base. All boundaries are non-flux boundaries except for the borehole on which a constant fluid injection rate is applied. The fluid injection rate in the experiments is 30 ml min^{-1}. The water and supercritical CO_2 fracturing experiments were conducted in a thermal bath, kept at 60 °C (333.15 K). Input parameters for the simulations are listed in Table 2 (Ma et al., 2016; Wu et al., 2016; Zhang et al., 2017) (see Fig. 7).

Fig. 8 shows the comparisons of experimental and numerical results in the case where the three fluids (water, liquid CO_2, and supercritical CO_2) are injected into shale samples. This demonstrates, at least qualitatively, that fracturing by supercritical CO_2 is a viable method to introduce improved complexity in fracturing. According to Fig. 8, fractures induced by supercritical CO_2 are irregular multiple branching fractures of different widths and lengths that form a complex fracture network. Supercritical CO_2 and liquid CO_2 can induce two or more transverse fractures, apparently as an "X"-shape or "Y"-shape fracture pattern, while fractures induced by hydraulic fracturing present themselves as a single main "I"-shape along a single plane. Furthermore, the width of supercritical CO_2 fractured cracks is larger than those of the cracks formed by liquid CO_2 and hydraulic fracturing. In terms of fracture morphology, supercritical CO_2 has an apparent advantage over liquid CO_2 and water fracturing. As shown in Fig. 9, the breakdown pressure of supercritical CO_2 is smaller than the pressures required for liquid CO_2 and water. What's more, not only the fracture patterns of numerical fracturing experiments but also the breakdown pressures compare well with the experimental observations. Therefore, it is reasonable to conclude that the proposed model is effective in simulating fracturing process.

5. Numerical simulation of fluid-driven fracturing

The two-dimensional fluid fracturing problem comprises a cross-section through a cubic specimen containing a vertical borehole (Fig. 10) and with an applied anisotropic stress field. The pressurizing fluids are two states of single-phase gas (supercritical and liquid CO_2) injected into the borehole until breakdown (unstable fracture propagation occurs) at a maximum pressure results. This may be represented in 2-D as a problem of plane strain and of transient state fluid flow.

5.1. Model geometry

According to the experiments conducted by Ishida et al. (2004, 2012), the geometries and loading conditions of the model are defined as shown in Fig. 10. The cubic rock specimen is 190 cm on edge with a 20 cm diameter borehole. The boundary conditions correspond to confining stresses applied on the top boundary (σ_1) and right boundary (σ_3) and rollers on opposite faces. All boundaries are non-flux boundaries except for the borehole on which a monotonic increasing fluid injection pressure is applied. In addition, in order to investigate the effects of principal stress and stress differences on fracturing process, $\lambda = \sigma_3/\sigma_1$ is defined to describe stress boundaries.

To representing the realistic heterogeneity in rock, we assume that the elastic modulus and strength follow the Weibull distribution. This takes the form of a probability density function as:

$$f(u) = \frac{m}{u_0}\left(\frac{u}{u_0}\right)^{m-1} \exp\left(-\left(\frac{u}{u_0}\right)^{m}\right) \tag{28}$$

where u is the elastic modulus or strength for the REV, u_0 is the average value of elastic modulus or strength and m describes the shape of the distribution function. In this study, the homogeneity index m is set to 5, and the other physico-mechanical parameters of the rock and fluids are assigned according to Table 3.

5.2. Phase response for CO_2

CO_2 is in a gaseous state at the beginning of the injection, and then becomes supercritical state when the temperature and pressure exceed the critical point (304.1 K and 7.38 MPa). The density-pressure curves for the three different liquids are shown in Fig. 11. Notably, the density of supercritical CO_2 increases significantly in the pressure range 6–10 MPa. According to Fig. 12, the first derivative of the density also changes

significantly when pressure exceeds critical pressure. This is an important feature/factor in our novel fracturing model, as shown in Eq. (19).

In the numerical simulation of supercritical CO_2 induced fracturing, the temperature T is kept at 318.15 K (45 °C) to ensure that the supercritical state will endure after the injection pressure reaches 7.38 MPa and before unstable fracture propagation occurs. For fracturing with liquid CO_2, the temperature is set to room temperature (293.15 K; 20 °C) and the vapor pressure may be evaluated as (Span and Wagner, 1996):

$$\ln\left(\frac{p_s}{p_c}\right) = \frac{T_c}{T}\left[\sum_{i=1}^{4} a_i\left(1-\frac{T}{T_c}\right)^{t_i}\right] \tag{29}$$

where p_s is the vapor pressure, T is the temperature, p_c and T_c are the critical pressure and temperature, respectively, with the other parameters remaining constant. Substituting $T = 293.15$ K to Eq. (29) yields a vapor pressure of 5.74 MPa.

To simplify the simulation, we assume that the dynamic viscosity of CO_2 remains unchanged until its phase state changes. In the numerical implementation, the phase state of CO_2 is determined by comparing the injection pressure with critical pressure and vapor pressure.

5.3. Numerical implementation of the model

This physical system is nonlinear both in space and time domain, precluding the possibility of an analytical solution. The complete set of coupled equations is solved by FEM. This approach requires that the damage variable and the damage-induced alterations in elastic modulus and permeability are continually updated with load. The summary of the basic procedures are as follows.

(1) After the establishment of the model geometry, the geomechanical model is discretized into a series of REVs. Then the initial mechanical and hydraulic properties are defined and the initial boundary conditions are applied.
(2) A fully coupled analysis is performed by FEM via COMSOL Multiphysics, and the stress, strain, and pore pressure for all the REVs are obtained.
(3) Effective stresses are calculated from Biot theory and Langmuir equation, are used to check if a damage threshold has been reached for the REVs (Eq. (25)).
(4) Effective stresses in the damaged REVs are substituted into Eq. (26) to calculate the damage variable. Then, the elastic modulus and permeability of these REVs are modified following Eqs. (25) and (27).
(5) The finite element model with the updated material parameters is analyzed and the result is compared with the prior state. If the damage zone extends, steps (3)–(5) are repeated, otherwise, step (6) is implemented.
(6) The boundary conditions are updated with the next load increment.

The fully coupled procedures are implemented in MATLAB to obtain the mechanical parameters related to damage and implemented into COMSOL Multiphysics, to complete the FEM analysis.

5.4. Evolution of fractures

We now focus on the evolution of fractures driven by the pressurization of supercritical CO_2 and compare them with those induced by liquid CO_2 and water. Figs. 13–15 display the evolving fracture patterns induced by supercritical CO_2, liquid CO_2, and water respectively. The fractures grow progressively in the direction of the maximum principal stress. However, due to the heterogeneity of the mechanical properties of the rock, the fracture patterns are relatively non-planar and irregular.

Comparing the fracture patterns induced by the three kinds of fluids, those induced by supercritical CO_2 are the most complex and are most widely distributed at any single injection (driving) pressure, followed by those induced by liquid CO_2 and then water. These results since there are many REVs with a relatively low strength in the region around the main fractures. As the fracturing fluids invade the rock, those REVs are ruptured by the increasing pore pressure and will coalesce into a main fracture as they self-connect. With a much lower dynamic viscosity, supercritical CO_2 can flow rapidly and transfer the pore pressure distal from the borehole, rather than liquid CO_2 and water under the same injection pressure. This makes the fracture patterns complex and widely distributed. More importantly, compared to liquid CO_2 and water, supercritical CO_2 has a greater adsorptive potential, which eventually creates larger internal swelling stresses and induces larger damage. This is consistent with experimental observations in the literature (Ishida et al., 2004, 2012; Ranathunga et al., 2016).

5.5. Critical pressures and the effect of dynamic viscosity on fracturing

In order to investigate the critical pressures resulting in breakdown, we calculate the ratio of the area of the damage zone to the total area. According to experimental observations, there are two critical pressures to distinguish the different stages of the hydraulic fracturing processes (Detournay and Carbonell, 1994). One is the fracture initiation pressure, from which the fractures begin to propagate, and the other is the breakdown pressure, under which unstable fracture propagation occurs. Fig. 16 shows the variations of $S_{Damage\ area}/S_{Total}$ with different load steps during fracturing by water, liquid CO_2, and supercritical CO_2. Supercritical CO_2 fracturing produces a larger relative damage zones than that due to liquid CO_2 and water fracturing. Otherwise, liquid CO_2 fracturing only has a slight advantage over water fracturing. Supercritical CO_2, with the lowest viscosity penetrates the cracks more rapidly than either liquid CO_2 or water. As a result, supercritical CO_2 has the lowest fracture initiation pressure, followed by liquid CO_2 and then water.

Similarly, supercritical CO_2 has the lowest breakdown pressure, followed by liquid CO_2 and water. Actually, the difference in the fracture initiation pressures between supercritical CO_2, liquid CO_2, and water is not obvious. While, the breakdown pressures of supercritical CO_2, liquid CO_2, and water are significantly different.

Fig. 17 presents the results of fracture initiation pressure and breakdown pressure for the specimens with water, liquid CO_2, and supercritical CO_2. It is demonstrated that with increasing dynamic viscosity, the breakdown pressure increases significantly but the fracture initiation pressure increases only slightly. This can also be explained since the fluids with lower dynamic viscosity can flow farther under the same injection pressure, with observation supported by experimental observations (Ishida et al., 2004, 2012; Garagash and Detournay, 1997). In addition, the stress difference has a significant effect on fracture initiation pressure and breakdown pressure. The greater the stress difference is, the smaller the fracture initiation pressure is, and more easy to fracture.

5.6. The effect of pore pressure on breakdown pressure

In this section, a series of numerical simulations are conducted to investigate the effect of initial pore pressure on breakdown pressure. An increase of pore pressure can decrease static friction and thereby facilitate fracture propagation on favourably oriented planes, when deviatoric stress field is present. As shown in Fig. 18, in the numerical simulations, the resulting P_b-P_0 of Supercritical CO_2 fracturing is significantly different from water-based fracturing. For the water-based fracturing, the resulting P_b-P_0 linearly decreased with the increase of initial pore pressure. However, for the Supercritical CO_2 fracturing, the resulting P_b-P_0 indicated a nonlinear decrease with the increase of initial pore pressure. The effects of Supercritical CO_2 penetration complicates the explanation of the fracturing process. The Supercritical CO_2 penetration not only changes the pore pressure in the formation, but also the adsorption-

induced strain alters the mechanical properties of the formation.

6. Conclusions

Currently, water with additives is the primary fluid used in commercial shale gas and oil reservoir stimulation. However, the continued use of water as a fracturing fluid poses some problems. These relate to water-availability, post-fracturing treatment and disposal. In the foregoing, we present a novel coupled model using supercritical CO_2 as a fracturing fluid for shale gas production. This is based on linking fluid flow, adsorption-induced internal swelling stress, solid deformation and damage into a distributed-parameter model. According to various numerical experiments, the following conclusions are drawn.

Based on the microcrack model representing shales with low porosity, the analytical and numerical results show that the effective stress coefficient is much smaller than unity. The patterns of fractures induced by supercritical CO_2 are more complex and more widely distributed than those induced by liquid CO_2 and water under the same injection pressure. This may be partly due to the lower dynamic viscosity of the supercritical fluid that can flow and project pore pressures further from the borehole. Moreover, supercritical CO_2 has a greater adsorptive potential, which eventually creates larger internal swelling stresses and induces larger damage. In addition, fractures grow progressively in the direction of the maximum principal stress. Due to the heterogeneity of rock mechanical properties, the fracture patterns are relatively irregular.

The dynamic viscosity of fracturing fluid has a great effect on the breakdown pressure. Supercritical CO_2 fracturing indeed has a lower fracture initiation pressure and a much lower breakdown pressure, as observed in experiments. With increasing dynamic viscosity, the breakdown pressure increases significantly, explained as above. However, the fracture initiation pressure only rises slightly as the dynamic viscosity increases. Furthermore, the stress difference also has a significant impact on fracture initiation pressure and breakdown pressure. The greater the stress difference is, the smaller the fracture initiation pressure and breakdown pressure are. The effects of Supercritical CO_2 penetration complicates the explanation of the fracturing process. For the Supercritical CO_2 fracturing, the resulting P_b-P_0 nonlinearly decreased with the increase of initial pore pressure. The Supercritical CO_2 penetration not only changes the pore pressure in the formation, but also the adsorption-induced damage alters the mechanical properties of the formation.

Acknowledgements

This work is funded by the National Key Research and Development Program of China (Grant No. 2016YFC0801607), National Science Foundation of China (Grant Nos. 51525402, 51374049, and 51574060), and the Fundamental Research Funds for the Central Universities of China (Grant Nos. N160103005 and N160104008). The authors also gratefully acknowledge financial support from China Scholarship Council. These supports are gratefully acknowledged.

References

Al-Anazi, H.A., Pope, G.A., Sharma, M.M., Metcalfe, R.S., 2002. Laboratory measurements of condensate blocking and treatment for both low and high permeability rocks. In: SPE Annual Technical Conference and Exhibition.

Alpern, J.S., Marone, C.J., Elsworth, D., Belmonte, A., Connelly, P., 2012. Exploring the physicochemical processes that govern hydraulic fracture through laboratory experiments. In: Proceedings of 46th US Rock Mechanics/Geomechanics Symposium. Chicago.

API, 2010. Water Management Associated with Hydraulic Fracturing.

Biot, M.A., 1941. General theory of three-dimensional consolidation. J. Appl. Phys. 12, 155–164.

Carroll, M.M., 1979. An effective stress law for anisotropic elastic deformation. J. Geophys. Res. 84 (B13), 7510–7512.

Davies, R.J., Mathias, S.A., Moss, J., Hustoft, S., Newport, L., 2012. Hydraulic fractures: how far can they go? Mar. Petrol. Geol. 37 (1), 1–6.

Detournay, E., Carbonell, R., 1994. Fracture-mechanics analysis of the breakdown process in minifracture or leak-off tests. In: Proceedings of the 2nd Joint SPE/ISRM Rock Mechanics Conference: Rock Mechanics in Petroleum Engineering.

Elices, M., Guinea, G.V., Gómez, J., Planas, J., 2002. The cohesive zone model: advantages, limitations and challenges. Eng. Fract. Mech. 69 (2), 137–163.

Ellsworth, W.L., 2013. Injection-induced earthquakes. Science 341 (6142), 142.

Elsworth, D., Spiers, C.J., Niemeijer, A.R., 2016. Understanding induced seismicity. Science 354 (6318), 1380–1381.

EPA, 2010. Hydraulic Fracturing Research Study.

Gan, Q., Elsworth, D., Alpern, J.S., Marone, C., Connolly, P., 2015. Breakdown pressures due to infiltration and exclusion in finite length boreholes. J. Petrol. Sci. Eng. 127, 329–337.

Garagash, D., Detournay, E., 1997. An analysis of the influence of the pressurization rate on the borehole breakdown pressure. Int. J. Solid Struct. 34 (24), 3099–3118.

Pijaudier-Cabot, G., 2013. Shale Gas: Any Alternatives to Hydraulic Fracturing? http://www.paristechreview.com/2013/01/14/hydraulic-fracturing/ [accessed September 2016].

Griffith, A.A., 1921. The phenomena of rapture and flow in solids. Trans. Roy. Soc. London. Series A 221, 163–198.

Gupta, D.V.S., Bobier, D., 1998. The history and success of liquid CO_2 and CO_2/N_2 fracturing system. SPE, 40016, 15–18.

Gupta, S., 2011. Unconventional fracturing fluids: what, where and why. In: Technical Workshops for the Hydraulic Fracturing Study. US EPA, Arlington, VA.

GWPC, 2009. Modern Shale Gas Development in the United States: a Primer. US Department of Energy, Office of Fossil Energy.

Heller, R., Zoback, M., 2014. Adsorption of methane and carbon dioxide on gas shale and pure mineral samples. J. Unconv. Oil Gas Resour. 8, 14–24.

Ishida, T., Aoyagi, K., Niwa, T., Chen, Y., Murata, S., Chen, Q., Nakayama, Y., 2012. Acoustic emission monitoring of hydraulic fracturing laboratory experiment with supercritical and liquid CO2. Geophys. Res. Lett. 39 (16), 16309.

Ishida, T., Chen, Q., Mizuta, Y., Roegiers, J.C., 2004. Influence of fluid viscosity on the hydraulic fracturing mechanism. J. Energ. Resour. Asme 126 (3), 190–200.

Jackson, R.E., Gorody, A.W., Mayer, B., Roy, J.W., Ryan, M.C., Van Stempvoort, D.R., 2013. Groundwater protection and unconventional gas extraction: the critical need for field-based hydrogeological research. Ground Water 51 (4), 488.

Javadpour, F., 2009. Nanopores and apparent permeability of gas flow in mudrocks (shales and siltstone). J. Can. Pet. Technol. 48 (8), 16–21.

Jung, J.W., Espinoza, D.N., Santamarina, J.C., 2015. Properties and phenomena relevant to CH_4-CO_2 replacement in hydrate-bearing sediments. J. Geophys. Res. 115, B10102.

Li, X., Elsworth, D., 2015. Geomechanics of CO_2 enhanced shale gas recovery. J. Nat. Gas Sci. Eng. 26, 1607–1619.

Ma, Y., Pan, Z., Zhong, N., Connell, L.D., Down, D.I., Lin, W., Zhang, Y., 2016. Experimental study of anisotropic gas permeability and its relationship with fracture structure of Longmaxi Shales, Sichuan Basin, China. Fuel 180, 106–115.

Mahadevan, J., Sharma, M.M., Yortsos, Y.C., 2007. Capillary wicking in gas wells. SPE J. 12, 429–437.

Middleton, R., Viswanathan, H., Currier, R., Gupta, R., 2014. CO_2 as a fracturing fluid: potential for commercial-scale shale gas production and CO_2 sequestration. Energy Procedia 63, 7780–7784.

Middleton, R.S., Carey, J.W., Currier, R.P., Hyman, J.D., Kang, Q.J., Karra, S., Jimenez-Martinez, J., Porter, M.L., Viswanathan, H.S., 2015. Shale gas and non-aqueous fracturing fluids: opportunities and challenges for supercritical CO2. Appl. Energy 147, 500–509.

Middleton, R.S., Keating, G.N., Stauffer, P.H., Jordan, A.B., Viswanathan, H.S., Kang, Q.J.J., Carey, J.W., Mulkey, M.L., Sullivan, E.J., Chu, S.P.P., Esposito, R., Meckel, T.A., 2012. The cross-scale science of CO_2 capture and storage: from pore scale to regional scale. Energ. Environ. Sci. 5 (6), 7328–7345.

Nur, A., Byerlee, J.D., 1971. An exact effective stress law for elastic deformation of rock with fluids. J. Geophys. Res. 16 (26), 6414–6419.

Olson, J.E., 2008. Multi-fracture propagation modeling: applications to hydraulic fracturing in shales and tight gas sands. In: Proceedings of the 42nd US Rock Mechanics. San Francisco.

Parekh, B., Sharma, M.M., 2004. Cleanup of water blocks in depleted low-permeability reservoirs. In: SPE Annual Technical Conference and Exhibition.

Ranathunga, A.S., Perera, M.S.A., Ranjith, P.G., Bui, H., 2016. Super-critical CO_2 saturation-induced mechanical property alterations in low rank coal: an experimental study. J. Supercrit. Fluids 109, 134–140.

Ren, L., Su, Y., Zhan, S., Hao, Y., Meng, F., Sheng, G., 2016. Modeling and simulation of complex fracture network propagation with srv fracturing in unconventional shale reservoirs. J. Nat. Gas Sci. Eng. 28, 132–141.

Rogers, S., Elmo, D., Dunphy, R., Bearinger, D., 2010. Understanding hydraulic fracture geometry and interactions in the Horn River Basin through DFN and numerical modeling. SPE 137488. In: Proceedings of Canadian Unconventional Resources and International Petroleum Conference. Calgary.

Scanlon, B.R., Reedy, R.C., Nicot, J.P., 2014. Comparison of water use for hydraulic fracturing for unconventional oil and gas versus conventional oil. Environ. Sci. Technol. 48 (20), 12386–12393.

Sheng, G.L., Su, Y.L., Wang, W.D., Liu, J.H., Lu, M.J., Zhang, Q., Ren, L., 2015. A multiple porosity media model for multi-fractured horizontal wells in shale gas reservoirs. J. Nat. Gas Sci. Eng. 27, 1562–1573.

Span, R., 2000. Multi Parameter Equation of State: an Accurate Source of Thermodynamic Property Data. Springer-Verlag Press, Germany, pp. 15–56.

Span, R., Wagner, W., 1996. A new equation of state for carbon dioxide covering the fluid region from the triple-point temperature to 1100 K at pressure up to 800 MPa. J. Phys. Chem. Ref. Data 25, 1509–1596.

Stauffer, P.H., Keating, G.N., Middleton, R.S., Viswanathan, H.S., Berchtold, K.A., Singh, R.P., Pawar, R.J., Mancino, A., 2011. Greening coal: breakthroughs and challenges in carbon capture and storage. Environ. Sci. Technol. 45 (20), 8597–8604.

Terzaghi, K. Van, 1923. Die Berechung ser Durchzssigheitsziffer des Tones aus dem Verlauf der hydrodynamischen Spannungserscheinungen, Sitzungsber. Akad. Wiss. Wien Math Naturwiss. Kl. Abt. 2A (132), 105.
Vidic, R.D., Brantley, S.L., Vandenbossche, J.M., Yoxtheimer, D., Abad, J.D., 2013. Impact of shale gas development on regional water quality. Science 340 (6134), 1235009.
Walsh, J.B., 1965. The effect of cracks on the compressibility rock. J. Geophys. Res. 70 (2), 381–389.
Wang, H., Li, G., Shen, Z., 2012. A feasibility analysis on shale gas exploitation with supercritical carbon dioxide. Energy Sources 34 (15), 1426–1435.
Wang, J.H., Elsworth, D., Zhu, W.C., Liu, J.S., Wu, Y., 2015. The influence of fracturing fluids on fracturing processes: a comparison between gas and water. In: Proceedings of the 49th US Rock Mechanics/Geomechanics Symposium. San Francisco.
Wu, K., Li, X., Wang, C., Chen, Z., Yu, W., 2015. A model for gas transport in microfractures of shale and tight gas reservoirs. AIChE J. 61 (6), 2079–2088.
Wu, Y., Li, X., He, J., Zheng, B., Sciubba, E., 2016. Mechanical properties of Longmaxi black organic-rich shale samples from south China under uniaxial and triaxial compression states. Energies 9 (12), 1088.
Ye, Z., Janis, M., Ghassemi, A., Riley, S., 2017. Laboratory investigation of fluid flow and permeability evolution through shale fractures. In: Proceedings of Unconventional Resources Technology Conference. Austin, Texas.
Yuan, B., Su, Y.L., Moghanloo, R.G., Rui, Z.H., Wang, W.D., Shang, Y.Y., 2015b. A new analytical multi-linear solution for gas flow toward fractured horizontal wells with different fracture intensity. J. Nat. Gas Sci. Eng. 23, 227–238.
Yuan, B., Wood, D.A., Yu, W., 2015a. Stimulation and hydraulic fracturing technology in natural gas reservoirs: theory and case studies (2012–2015). J. Nat. Gas Sci. Eng. 26, 1414–1421.
Yuan, B., Zheng, D., Moghanloo, R.G., Wang, K., 2017. A novel integrated workflow for evaluation, optimization, and production predication in shale plays. Int. J. Coal Geol. 180, 18–28.
Zhang, X.W., Lu, Y.Y., Tang, J.R., Zhou, Z., Liao, Y., 2017. Experimental study on fracture initiation and propagation in shale using supercritical carbon dioxide fracturing. Fuel 190, 370–378.
Zhu, W.C., Liu, L.Y., Liu, J., Wei, C.H., Peng, Y., 2018. Impact of gas adsorption-induced coal damage on the evolution of coal permeability. Int. J. Rock Mech. Min. 101, 89–97.
Zhu, W.C., Tang, C.A., 2004. Micromechanical model for simulating the fracture process of rock. Rock Mech. Rock Eng. 37 (1), 25–56.